Using the Physically Based Constitutive Model and Processing Maps to Understand the Hot Deformation Behavior of 2304 Lean Duplex Stainless Steel

Oleary Bill[1,*], Charles Siyasiya[1] & Joseph Moema[2]

[1]Department of Materials Science and Metallurgical Engineering, University of Pretoria, Hatfield, Pretoria, 0028, South Africa

[2]Advanced Materials Division (AMD), Mintek, 200 Malibongwe Drive, P Bag X 3015, Randburg, 2125, South Africa

*Correspondence to Oleary Bill. e-mail: oleary.bill@up.ac.za; moshebill80@gmail.com

Abstract

The hot deformation behavior of 2304 lean duplex stainless steel was investigated by means of processing maps and physically based constitutive modeling in the temperature range of 850 °C to 1050 °C and strain rate of 0.1 to 15 s^{-1}. For all the processing maps developed for strains of 0.1 to 0.6, dynamic restoration mechanisms were efficient in preventing flow instability at low strain rates (1 to 4 s^{-1}) in the studied temperature range. Hot deformation at medium strain rates of 5 to 7 s^{-1} results in the risk of flow instability. However, for typical industrial purposes, there is a possibility of hot working at higher strain rates (10 s^{-1} and above) at lower temperatures without the risk of instability by promoting dynamic recrystallization in the austenitic phase of the steel. The flow behavior of the steel can be accurately modeled by coupling the Estring-Mecking constitutive equation (for the work hardening and recovery region) with the Avrami model, which captures the dynamic recrystallization region.

1 Introduction

Duplex stainless steels find use in diversified fields ranging from petroleum refining to ocean industries due to their attractive combination of strength, toughness and high corrosion resistance.[1,2] These properties stem from the two-phase microstructure due to the presence of austenite and ferrite, in almost equal amounts.[3] However, compared to their single-phase counterparts, the dual phase steels present co-existence of crystal structures and stacking fault energy (SFE) values owing to the presence of austenite and ferrite at high temperatures.[4,5,6] This complicates the response of the two phases to external loading at high temperatures and in turn results in complicated deformation behavior of the steel. Single-phase ferrite is characterized by a high SFE and therefore exhibits extensive dynamic recovery (DRV).[7,8] On the other hand, austenite has a low SFE thereby bears DRV and thereby further softens by dynamic recrystallization (DRX).[9,10] However, in the duplex structure the presence of the other phase considerably affects the deformation behavior of each constituent phase.[11] Thus, the total strength of the duplex stainless steel is a result of contribution of the ferrite and the austenite depending on the amount of strain that is partitioned in each phase. The strain as well as the stress partitioning of duplex steels based on single phases can be calculated from a rule of mixture.[12] It has been affirmed in another study that at the early stages of deformation, strain is mostly accommodated in the δ-ferrite phase and transferred to austenite where it can accumulate and trigger dynamic recrystallization.[13] Higher temperatures and low strain rates promote DRV in ferrite and result in a plateau after work-hardening stage because of delayed load transfer while low temperatures and high strain rates restrict DRV in ferrite and rapid

transfer of load to austenite takes place.[14] However, the hot working behavior of duplex stainless steels still presents challenges especially on predicting the optimum processing window for these steels.

This is a processing window that is crucial in achieving the outcomes of the desired thermomechanical process without flow instabilities. Flow instabilities compromise the mechanical and microstructural integrity of the material being hot worked. These flow instabilities usually manifest themselves microstructurally in the form of flow localization, adiabatic shear band formation, mechanical twinning, and kinking or flow rotations.[15] In any case, they are an indication that the specific flow localization parameter of the material being hot deformed has been exceeded. Typically, as a result of these microstructural instabilities and deformation adiabatic heating, flow softening does take place during hot working, and this can easily be interpreted to be from dynamic recrystallization. To operate within the limits of thermo-mechanical processing where flow localization and hence flow instability do not occur, the hot working window needs to be defined. This can be done through processing maps of the material based on a dynamic material model (DMM) following the extensive work by Prasad and Seshacharyulu.[16]

In the dynamic material model, a work piece undergoing hot deformation is considered to be a power dissipator. The power absorbed P by the material during plastic deformation is dissipated through two complementary processes: viscoplastic heat or temperature rising (G part) and microstructural changes (J part), expressed mathematically as[16]:

$$P = J + G = \sigma\dot{\varepsilon} = \int_0^{\sigma} \dot{\varepsilon}\,\mathrm{d}\sigma + \int_0^{\varepsilon} \sigma\,\mathrm{d}\dot{\varepsilon} \tag{1}$$

The efficiency η of this power dissipation process is calculated at a constant strain as follows:

$$\eta = \frac{J}{J_{\max}} = \frac{2m}{m+1} \tag{2}$$

where m is the strain rate sensitivity of the material, and $m = 1$, where $J = J_{\max} = \sigma\dot{\varepsilon}/2 = p/2,$ for an ideal linear dissipater. The strain rate sensitivity is calculated from the usual equation:

$$m = \left.\frac{\partial \ln \sigma}{\partial \ln \dot{\varepsilon}}\right|_{\varepsilon,T} \approx \left.\frac{\Delta \log \sigma}{\Delta \log \dot{\varepsilon}}\right|_{\varepsilon,T} \tag{3}$$

where the terms σ, ε and T represent stress, strain and absolute temperature, respectively. The power dissipation map is constructed from the variation of efficiency η with the processing parameters of temperature, strain rate and strain.

While the power dissipation map shows the specific microstructure formation mechanism, another mechanism of importance during hot working is microstructure instability, *i.e.*, the region where this takes place also needs to be defined. Microstructure instability takes place when flow instability is negative, and this flow instability is given by the following equation[17]:

$$\xi = \frac{2m}{\eta} - 1 < 0 \tag{4}$$

A negative $\xi(\dot{\varepsilon})$ represents flow instability and its variation with temperature and strain rate constitutes an instability map. Superimposing an instability map with the power dissipation map results in the construction of a processing map from which the processing parameters during the hot working process can be optimized.[18,19]

According to Kocks-Mecking (KM) model, the interplay between storage and annihilation of dislocations as still being the main mechanism in the absence of DRX gives rise to the evolution of dislocation density, which can be expressed as follows:

$$\frac{\mathrm{d}\rho}{\mathrm{d}\varepsilon} = k_1\sqrt{\rho} - k_2\rho \tag{5}$$

$$\sigma = \alpha G_{\mathrm{m}} b\sqrt{\rho} \tag{6}$$

where α is a constant, b is the Burger's vector, G_{m} is the shear modulus, and ρ is the dislocation density.

From Eqs. [5] and [6], the evolution of dislocation density and flow stress can be expressed as[20]:

$$\theta = \theta_0\left(1 - \frac{\sigma}{\sigma_{\mathrm{s}}}\right) \tag{7}$$

Estrin and Mecking[21] considered the storage rate U to be constant and modified the Kocks-Mecking method above to give:

$$\frac{\mathrm{d}\rho}{\mathrm{d}\varepsilon} = U - \Omega\rho \tag{8}$$

where U represents the work hardening rate constant. The above equation can be rewritten in the following form:

$$\theta\sigma = A - B\sigma^2 \tag{9}$$

By integration of Eq. [9], the flow stress in the absence of softening (DRX) can be determined from the Estring-Mecking model as:

$$\sigma^{\mathrm{EM}} = \left[\sigma_{\mathrm{sat}}^2 + \left(\sigma_0^2 - \sigma_{\mathrm{sat}}^2\right)\exp\left(-2\mathrm{B}\varepsilon\right)\right]^{1/2}, \varepsilon < \varepsilon_{\mathrm{p}} \tag{10}$$

When softening due to DRX has taken place, the flow stress evolution between peak stress and steady-state stress, *i.e.*, flow stress beyond the peak strain (ε_{p}), can be determined from the following equation:

$$\sigma = \sigma^{\mathrm{EM}} - X\left(\sigma^{\mathrm{EM}} - \sigma_{\mathrm{ss}}\right), \varepsilon \geq \varepsilon_{\mathrm{p}} \tag{11}$$

where σ^{EM} is the stress predicted from the Esting-Mecking model, σ_{sat} is the saturation stress (maximum stress when DRV is the only softening mechanism at play), X is the DRX volume fraction, and σ_{ss} is the steady-state stress.

2 Materials and Methods

The material that was investigated in this study was 2304 Lean Duplex stainless steel (LDSS) in the form of a transfer bar having the chemical composition of 0.0 pct C, 22.39 pct Cr, 3.70 pct Ni, 0.37 pct Mo, 0.58 pct Si, 1.22 pct Mn, 0.17 pct Cu, 0.12 pct N, 0.01 pct Nb, 0.03 pct Ti, 0.13 pct V, 30 ppm S and the rest being Fe (all in mass pct).

Cylinders of 5 mm diameter and 10 mm length were machined from the 2304 LDSS transfer bar. Isothermal compression experiments were carried out in the Bahr 850D^{TM} Dilatometer. Alumina corundum dies were used in the deformation of the specimen, and these were expected to reduce the friction during deformation significantly. Five different temperatures (850 °C, 900 °C, 950 °C, 1000 °C and 1050 °C) and five different strain rates (0.1, 1, 5, 10 and 15 s^{-1}) were used up to a maximum strain of 0.8. The specimens were immediately quenched using helium after deformation, sliced along the compression axis and etched in Beraha etchant (100 ml H_2O, 30 ml HCl and 1.2 g $K_2S_2O_5$). Microstructural analyses were carried out using the Olympus-PMG3 optical microscope and an HKL electron backscattered diffraction (EBSD) attachment on a JEOL Oxford Tungsten Filament scanning electron microscope (SEM).

3 Results and Discussions

3.1 Experimental Characterization

Following the reheating at 1200 °C for 5 min and cooling to test temperature and soaking for 10 to 20 min to ensure a homogeneous microstructure and phase stability before deformation, minor variation was observed in the phase fraction between 850 °C and 1050 °C temperature range. The austenite phase (white) was observed to be 39 pct at 850 °C and 35 pct at 1050 °C as shown in Figure 1(a) and (b), respectively. The strain partitioning between the two phases during deformation can thus be considered to be almost equal in the studied temperature range, and the effect of temperature on strain partitioning was considered to be negligible in the study.

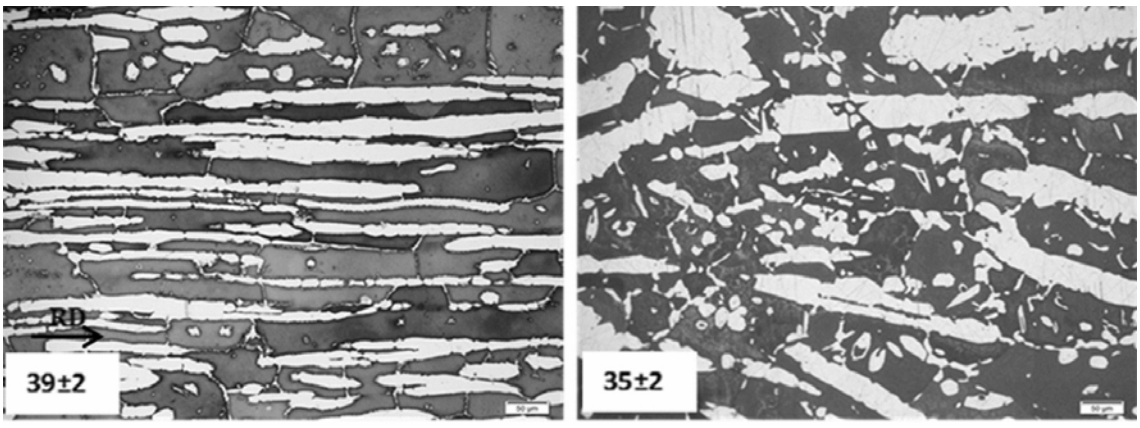

Fig. 1. Microstructures after annealing at different temperatures for 1200 s and quenching to achieve ferrite and austenite fraction for (*a*) 850 °C and (*b*) 1050 °C. Ferrite is depicted as black/gray and austenite as white. RD is the rolling direction of the transfer bar from which the samples were made

3.2 Hot Deformation Behavior

Figure 2(a) shows the true stress-strain curves of an isothermally deformed 230 LDSS at a deformation temperature of 850 °C and various strain rates. The flow stress can be observed to gradually increase to a less defined peak (σ_p) with increasing strain, followed by a continuous decrease in flow stress with no sign of attainment of steady-state at a strain of 0.6, with the exception of at a strain rate of 10 s^{-1}. No correction for temperature was carried out as the temperature increase during each deformation was too negligible to cause any softening as can also be seen in the identical softening for the strain rates of 0.1 to 15 s^{-1}, with more DRX at 10 s^{-1}.

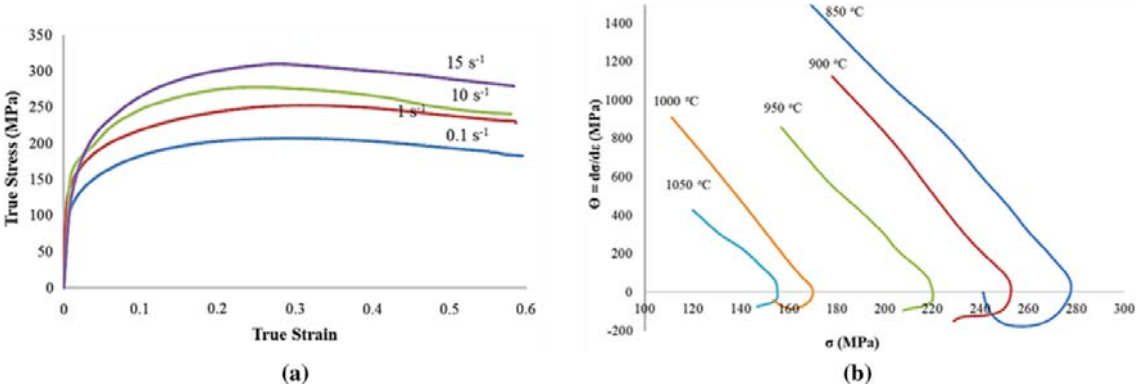

Fig. 2. (*a*) Flow curves of 2304 DSS hot deformed at 850 °C and different strain rates; (*b*) work hardening curves (Kocks-Mecking plots) of 2304 DSS hot deformed at a strain rate of 10 s^{-1} and different temperatures

Typical Kocks-Mecking plots (θ–σ curves) of the 2304 LDSS at a strain rate of 10 s^{-1} and various temperatures are shown in Figure 2(b). A linear decrease of θ can be initially observed for a short interval. However, of interest is the absence of a clear plateau and inflection point which is commonly observed in single-phase steels to represent critical stress (σ_c) and signal the onset of DRX,[9] especially at a temperature of 850 °C. This behavior can be attributed to the presence of a multiphase microstructure and flow localization resulting in a work hardening rate generally different from that of single-phase steels.[22,23] The different restoration behaviors in ferrite and austenite in addition to partitioning of stress and strain between the two constituents need to be considered when modeling the flow curves of DSS.

In Figure 2(b), the work hardening curve at 850 °C cuts the *x*-axis, typical of when steady-state stress has been attained. Thus, the value of the asymptotic stress at saturation, σ_{sat}, which on further straining is a representation of dislocation density of the most work hardened grains and the driving force for continuation of dynamic recrystallization, is derived from the KM model. This is achieved through the fitting and smoothing part of the plastic strain section of the hot deformation flow curve with a polynomial function. A differential function is then obtained from the curves free of irregularities and fluctuations in order to have θ *vs* σ plots (Figure 2(b)) from which σ_{sat} is determined from the extrapolation of the linear portion of the θ–σ plot below the critical stress to $\theta = 0$.

3.3 Processing Maps

The processing maps obtained in the work hardening region of hot working (*i.e.*, $\varepsilon < \varepsilon_p = 0.3$) are shown in Figure 3. Thus, the two processing maps are for strains of 0.1 and 0.2, respectively. The efficiency of power dissipation is expressed in terms of a dimensionless

parameter η measured as a percentage. The variation of η with strain rate and temperature gives a power dissipation map. The flow instability domains which are predicted to occur when the dimensionless instability parameter \(\xi (\dot{\varepsilon }) < 0\) are indicated by shaded regions. A change in strain does not have much effect on the peak efficiency of the power dissipation (η). Two domains having equal peak efficiencies were observed at each strain, 43 and 42 pct for 0.1 and 0.2 strains, respectively. High efficiency of power dissipation is associated with the material dissipating more energy for microstructural changes beneficial to hot deformation such as DRV and DRX.[24] However, a high efficiency of power dissipation could alternatively be a result of unstable flow, which can be manifested as cracks and/or deformation bands.[18,25] Thus, analysis of the processing maps is done in combination with the microstructural observations. Microstructural observations from EBSD in Figure 4 show a high density in low angle grain boundaries (LAGB) especially at a strain rate of 10 s^{-1}, which in turn in this region corresponds to an instability region (negative efficiency) in the processing map. This can be an indication of the process of DRV not being favored at these deformation conditions as confirmed by a high density of dislocations. Hence, the peak efficiencies observed at temperatures of approximately 900 °C and 1000 °C, and strain rates of 2 and 3 s^{-1} at both strains of 0.1 and 0.2, respectively, are attributed to DRV in ferrite as the process is favored by high temperatures and low strain rates. At high strain rates (\(\dot{\varepsilon }\) > 5 s^{-1}), low and negative efficiency values are observed, in addition to flow instability (shaded areas), and this can be attributed to the rate at which the dislocations are generated surpassing the DRV rate. This then results in the build-up of deformation strain in ferrite and minimal transfer to austenite where minimal DRX takes place as confirmed by work hardening curves.

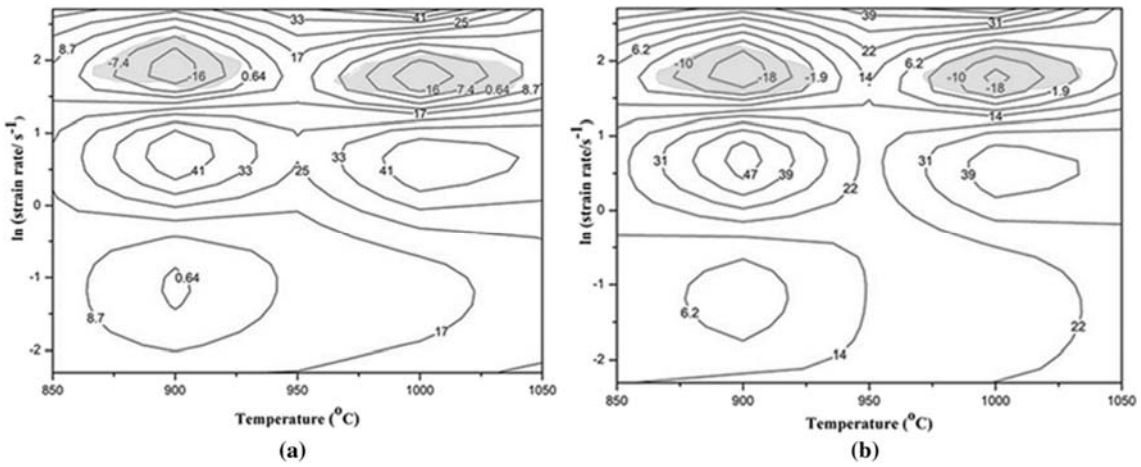

Fig. 3. Processing maps for 2304 LDSS at a true strain value of: (*a*) 0.1 and (*b*) 0.2. Contour numbers represent percent efficiency of power dissipation. Shaded regions correspond to flow instability

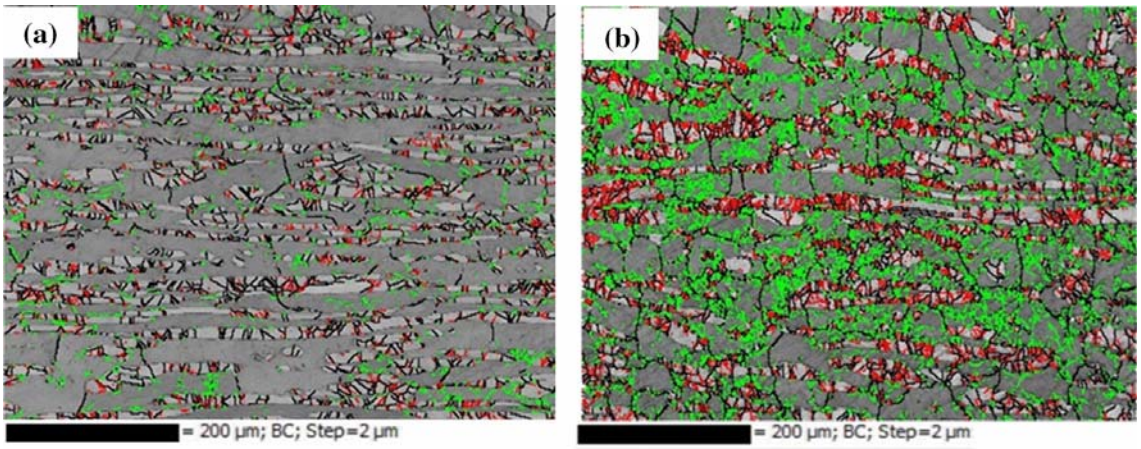

Fig. 4. Subgrain and grain structures at 850 °C with a strain rate of 10 s^{-1} with strains of: (*a*) 0.1; (*b*) 0.2. Green and red represent low angle grain (LAGB) boundaries in ferrite and austenite, respectively. HAGBs are shown by black color in both phases (Color figure online)

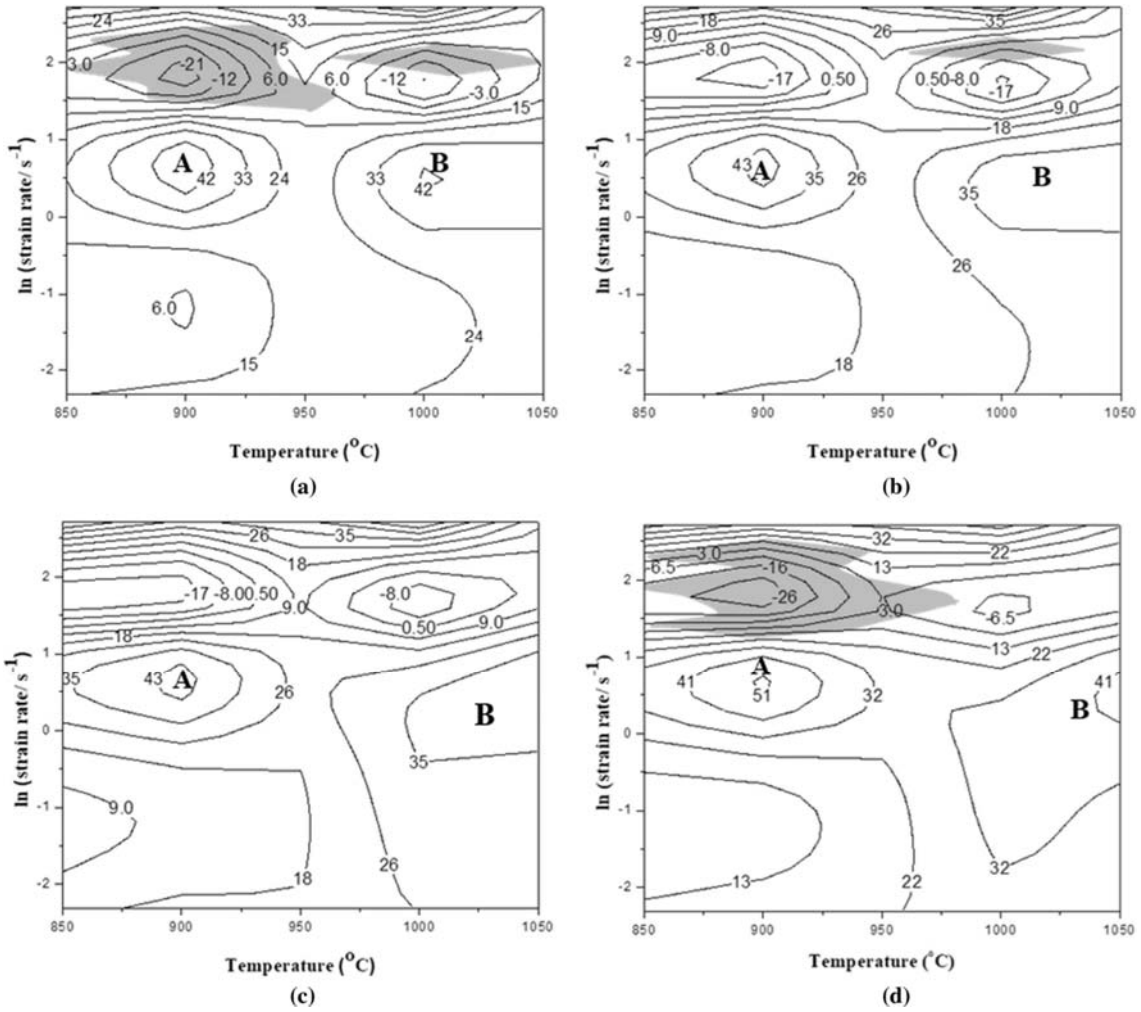

Fig. 5. Processing maps for 2304 LDSS at true strain values of: (*a*) 0.3, (*b*) 0.4, (*c*) 0.5, (*d*) 0.6. Contour numbers represent percent efficiency of power dissipation. Shaded regions correspond to flow instability

Figures 5(a) through (d) shows the processing maps for the 2304 LDSS deformed at the strain of 0.3, 0.4, 0.5 and 0.6, respectively. The peak strain was determined to be approximately 0.3. The peak efficiency in the two domains A and B in the work hardening region up to the peak strain show a slight change from strains of 0.1 and 0.2; however, at these high strains the power dissipation mechanism is most likely to be still DRV in ferrite with some contribution from little DRX in austenite as can be seen from the extended flow stability region at low strain rates. The regions of instability are still around strain rates of 5 to 7 s^{-1} over the entire temperature range. The current study mainly focused at the microstructural stability during the processing of the 2304 duplex stainless steel, hence the processing maps at different strains and the corresponding microstructures at 15 s^{-1} (typical processing strain rate in plant). It will be of further interest to also confirm the microstructural changes associated with high efficiency of power dissipation at low strain rates.

At a strain of 0.4 and 0.5 peak efficiencies are still comparable to those of strains below the peak strain ($\varepsilon = 0.3$) for domain A. The peak efficiency however increases sharply to 51 pct at a strain of 0.6 compared to lower strains where it is approximately 43 pct throughout. The increase in efficiency at higher strain can be attributed to more load being transferred from the softer ferrite phase to the harder austenite phase at higher strains, which triggers more DRX in austenite at low temperature and strain rate. For domain B, the peak efficiency however continues to vary. The variation in peak efficiencies at a given strain rate and strain (domains A and B) is due to the amount of the ferrite and austenite phases, which vary with temperature. The regions where the efficiency of power dissipation is negative are invariant with strain and constantly coincide with regions of unstable flow. An interesting observation at peak strain and beyond is the efficiency at temperature of 850 °C and higher strain rates of 10 s^{-1} and above. This observation agrees with the study[26] where the austenite in duplex steels may have accelerated dynamic recrystallization because of accumulation of more strain with increasing strain rate at low temperatures, which is also confirmed by the work hardening curves in this study (Figure 2(b)). This presence of DRX at high strain rate and low temperature resulting in the observed positive efficiency in the processing maps is also confirmed microstructurally in Figure 6(a).

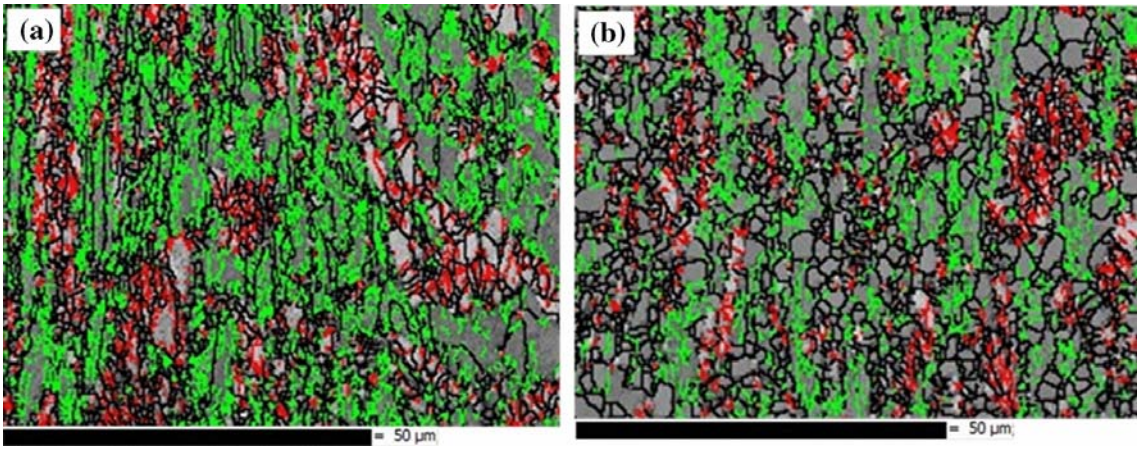

Fig. 6. Subgrain and grain structures at 15 s^{-1}: (*a*) 850 °C, (*b*) 1050 °C. Green and red represent low angle grain boundaries (LAGB) in ferrite and austenite, respectively. HAGBs are shown by black color in both phases (Color figure online)

Figure 6(a) also confirms that as the deformation temperature decreases and/or strain rate increases, the DRV in ferrite slows and the strain distribution to austenite takes place more

rapidly.[27] This in turn leads to DRX in austenite if the driving force nucleation is sufficient. On the other hand, conditions corresponding to very high strain rates and sufficiently high temperatures promote local presence of dynamic recrystallization in ferrite,[23] resulting in lower *Z* values and high efficiency of power dissipation as shown in Figure 6(b) and confirmed by the processing maps under the corresponding conditions.

3.4 Modeling the Flow Behavior of 2304 LDSS

To model the flow behaviors of duplex stainless steels where ferrite and austenite phases do coexist requires that the contribution of each phase be considered. The amount of strain that is partitioned in each phase will determine how much each phase will contribute to the total strength of the DSS. Thus, the law of mixture can be applied to model the flow behavior of the studied by considering the strain partitioning and the different strengths of the two phases. The following equations are used to develop the law of mixture:

$$\sigma_{\text{DSS}} = f_\gamma \sigma_\gamma + f_\alpha \sigma_\alpha \tag{12}$$

$$\varepsilon_{\text{DSS}} = f_\gamma \varepsilon_\gamma + f_\alpha \varepsilon_\alpha \tag{13}$$

where *f* represents the volume fraction and the indices γ and α refer to austenite and ferrite, respectively.

The softer phase, which is ferrite, accommodates the early stages of deformation such that at low strains:

$$\varepsilon_\gamma \approx 0 \text{ and } \left(\frac{1}{f_\alpha}\right)\varepsilon_{\text{DSS}} = (\varepsilon_\alpha)_{\max} \tag{14}$$

Equation [14] indicates the highest contribution of ferrite in ε_{DSS}. This contribution of ferrite decreases gradually at high strains and austenite gets to accommodate the greater part of plastic strain. Given the observed flow behavior in the study, it was assumed that the above rule of mixture holds and that ferrite contributes more at lower strains and WH + DRV characterizes the flow behavior; hence, the E-M model was applied. Tiny austenite islands were also seen dispersed in the ferrite matrix, which also justified the use of the E-M model.

The flow behavior in the WH + DRV regime, $\varepsilon < \varepsilon_p$, was modeled using the E-M model and for the flow softening after the peak, $\varepsilon > \varepsilon_p$, the Avrami model was used. These two models were then coupled to model the flow behavior of the steel over the entire region. The E-M model can predict the flow behavior up to peak, *i.e.*, WH + DRV region, and the KM approach can only predict the saturation stress.

Figure 7 shows that by coupling the E-M model and the Avrami model the overall flow behavior of the 2304 LDSS deformed can be modeled within reasonable accuracy and the parameters and constants used (obtained in Appendices 1 and 2) are indicated in Table I.

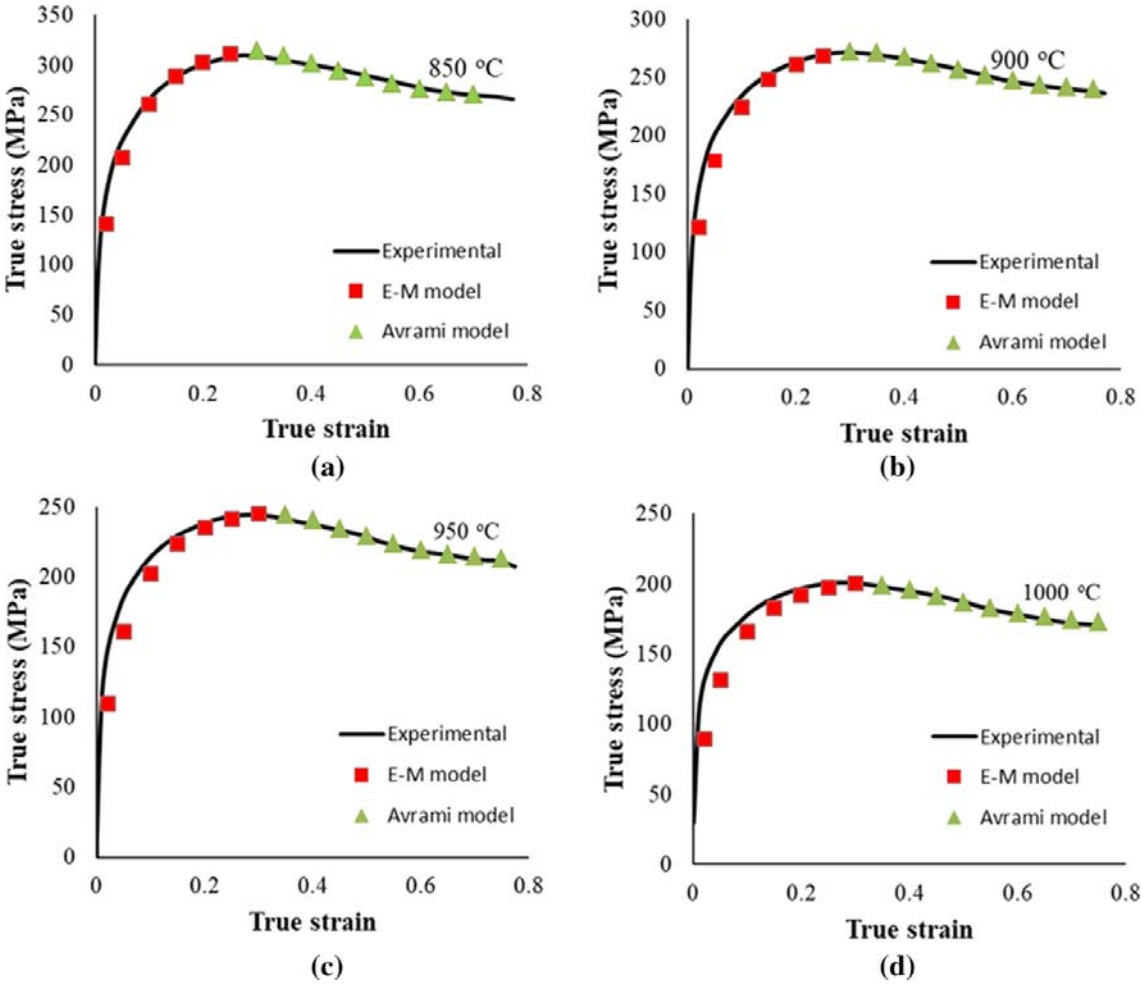

Fig. 7. Coupled Estrin-Mecking model and Avrami model for flow stress modeling at a 15 s^{-1} strain rate and different temperatures

Table I. Parameters and Constants Used for the Flow Stress from E-M WH + DRV Model ($\varepsilon < \varepsilon_p$) and Avrami Softening Model (ε \(\ge\) ε_p)

T (°C)	σ_{sat} (MPa)	σ_{ss} (MPa)	B	r	q
850	324	268	4.3	8.9	1.7
900	278	239	4.9	8.9	17
950	251	211	5.0	8.9	1.7
1000	204	136	5.4	8.9	1.7

4 Conclusions

From the study of the hot deformation behavior of the 2304 lean duplex stainless steel in the temperature range of 850 °C and 1050 °C and strain rate range of 0.1 and 15 s^{-1}, the following results were obtained:

1. Two domains with peak efficiencies of power dissipation are localized at temperatures of around 900 °C and 1000 °C at lower strains of 0.1 and 0.2. However, with increase in strain, these domains with peak efficiency continue manifesting in the temperature

range of 850 °C to 900 °C and 1000 °C to 1050 °C at strain rate range of 1 to 3 s^{-1}. Unstable domains can be observed around 900 °C and strain rate range of 5 to 9 s^{-1}. At higher strain rates and lower temperature flow stability is retained confirming that DRX in austenite is the main power dissipation mechanism at those conditions.
2. The modified EM model, which can predict the flow behavior of the steel up to peak strain, can be coupled to the Avrami equation to model the dynamic recrystallization by introducing a softening term.
3. Given the high strain rates of 11 to 35 s^{-1} in industrial practice, it can be concluded that the optimum temperature range without the risk of flow instability under such instances is 950 °C and 1000 °C.
4. The E-M work hardening model coupled to the Avrami model can sufficiently model the flow behavior of the 2304 LDSS.

Acknowledgments

The authors acknowledge Mintek for financial support through the DSI FMDN program, Columbus Stainless for the supply of materials and technical support and University of Pretoria for the use of the laboratories and equipment.

Research data for this article

The research data for this article are available on the University of Pretoria Bahr Dilatometer machine and the SEM post-processing machine, available on request.

References

1. A.I. Filho, J.M.D.A. Rollo, R. Silva, and G. Martinez: *Mater. Lett.*, 2005, vol. 59, pp. 1192–94. https://doi.org/10.1016/j.matlet.2004.12.026.
2. J.M. Cabrera, A. Mateo, L. Llanes, J.M. Prado, and M. Anglada: *J. Mater. Process Technol.*, 2003, vol. 143–144, pp. 321–25. https://doi.org/10.1016/S0924-0136(03)00434-5.
3. R. Badji, M. Bouabdallah, B. Bacroin, C. Kahloun, B. Belkessa, and H. Maza: *Mater. Charact.*, 2008, vol. 59, pp. 447–53. https://doi.org/10.1016/j.matchar.2007.03.004.
4. P. Cizek, B.P. Wynne, and W.M. Rainforth: *J. Micros.*, 2006, vol. 222, pp. 85–96. https://doi.org/10.1111/j.1365-2818.2006.01576.x.
5. P. Mao, K. Yang, and G. Su: *Mater. Sci. Technol.*, 2003, vol. 19, pp. 379–83. https://doi.org/10.1179/026708302225004793.
6. P. Cizek: *Acta Mater.*, 2016, vol. 106, pp. 129–43. https://doi.org/10.1016/j.actamat.2016.01.012.
7. C.M. Garzon and A.P. Tschiptschin: *Mater. Sci. Eng. A*., 2006, vol. 441, pp. 230–38. https://doi.org/10.1016/j.msea.2006.08.018.
8. P. Mao, K. Yang, and G. Su: *J. Mater. Sci. Technol.*, 2003, vol. 19, pp. 379–81.
9. J.J. Jonas, X. Quelennec, L. Jiang, and E. Martin: *Acta Mater.*, 2009, vol. 57, pp. 2748–56. https://doi.org/10.1016/j.actamat.2009.02.033.
10. A. Momeni, K. Dehghani, and G.R. Ebrahimi: *J. Alloys Compd.*, 2011, vol. 509, pp. 9387–93. https://doi.org/10.1016/j.jallcom.2011.07.014.
11. A. Momeni, K. Dehghani, and M.C. Poletti: *Mater. Chem. Phys.*, 2013, vol. 139, pp. 747–55. https://doi.org/10.1016/j.matchemphys.2013.02.026.
12. A. Quadfasel, J.A. Nietsch, M. Teller, and G. Hirt: *Metal.*, 2021, vol. 11, pp. 1–19. https://doi.org/10.3390/met11081285.

13. O. Balancin, W.A.M. Hoffman, and J.J. Jonas: *Metall. Mater. Trans. A*., 2001, vol. 31A, pp. 1353–64. https://doi.org/10.1007/s11661-000-0254-4.
14. A. Momeni and K. Dehghani: *Mater. Sci. Eng. A*., 2011, vol. 528, pp. 1448–54. https://doi.org/10.1016/j.msea.2010.11.020.
15. A.B. Li, L.J. Huang, Q.Y. Meng, L. Geng, and X.P. Cui: *Mater. Des.*, 2009, vol. 30, pp. 1625–31. https://doi.org/10.1016/j.matdes.2008.07.031.
16. Y.V.R.K. Prasad and T. Sesharyulu: *Mater. Sci. Eng. A*., 1998, vol. 243, pp. 832–88. https://doi.org/10.1016/S0921-5093(97)00782-X.
17. S.V.S. Narayana Murty, W.S. Sarma, and B. Nageswara Rao: *Metall. Mater. Trans. A*., 1997, vol. 28A, pp. 1581–82. https://doi.org/10.1007/s11661-997-0219-y.
18. Y.V.R.K. Prasad, K.P. Rao, and S. Sasidhara: *Hot Working Guide: A Compendium of Processing Maps*, 2nd ed. ASM International, Ohio, 2015.
19. S.V.S. Narayana Murty, B. Nageswara Rao, and B.P. Kashyap: *Mater. Sci. Technol.*, 2004, vol. 20, pp. 772–82. https://doi.org/10.1179/026708304225016671.
20. A. Laasraoui and J.J. Jonas: *Metall. Trans. A*., 1991, vol. 22, pp. 1545–57. https://doi.org/10.1007/BF02667368.
21. Y. Estrin and H. Mecking: *Acta Metall. A*., 1984, vol. 32, pp. 57–70. https://doi.org/10.1016/0001-6160(84)90202-5.
22. Q. Guo-Zhang: *In Tech*., 2013, https://doi.org/10.5772/54285.
23. S.B. Davenport, N.J. Silk, C.N. Sparks, and C.M. Sellars: *Mater. Sci. Technol.*, 2000, vol. 16, pp. 539–46. https://doi.org/10.1179/026708300101508045.
24. R.W. Evans and P.J. Scharning: *Mater. Sci. Technol.*, 2001, vol. 17, pp. 995–1004. https://doi.org/10.1179/026708301101510843.
25. Y.V.R.K. Prasad and K.P. Rao: *Mater. Sci. Eng. A*., 2005, vol. 31, pp. 141–50. https://doi.org/10.1016/j.msea.2004.08.049.
26. Y. Han, D. Zou, Z. Chen, G. Fan, and W. Zhang: *Mater. Charact.*, 2011, vol. 62, pp. 198–203. https://doi.org/10.1016/j.matchar.2010.11.013.
27. N. Haghdadi, D. Martin, and P. Hodgson: *Mater. Des.*, 2016, vol. 106, pp. 420–27. https://doi.org/10.1016/j.matdes.2016.05.118.

Appendices

Appendix 1: Derivation of the W.H. relations

According to the modified representation of the Estrin-Mecking model:

$$\theta\sigma = A - B\sigma^2 \tag{A1}$$

Integrating equation results in the equation for the flow stress in the WH + DRV regime according to the Estrin-Mecking modification given by:

$$\sigma^{\mathrm{EM}} = \left[\sigma_{\mathrm{sat}}^2 + \left(\sigma_0^2 - \sigma_{\mathrm{sat}}^2\right)\exp\left(-2\mathrm{B}\varepsilon\right)\right]^{1/2} \tag{A2}$$

where

$$\sigma_{\mathrm{sat}} = \sqrt{\frac{A}{B}} \tag{A3}$$

The constants in the above equation can be determined from the plot of product of the work hardening rate and stress, θ_σ, against the square of the stress, σ^2. From this plot A is the y-intercept and B the slope of the linear approximation of the plot (Figure A1).

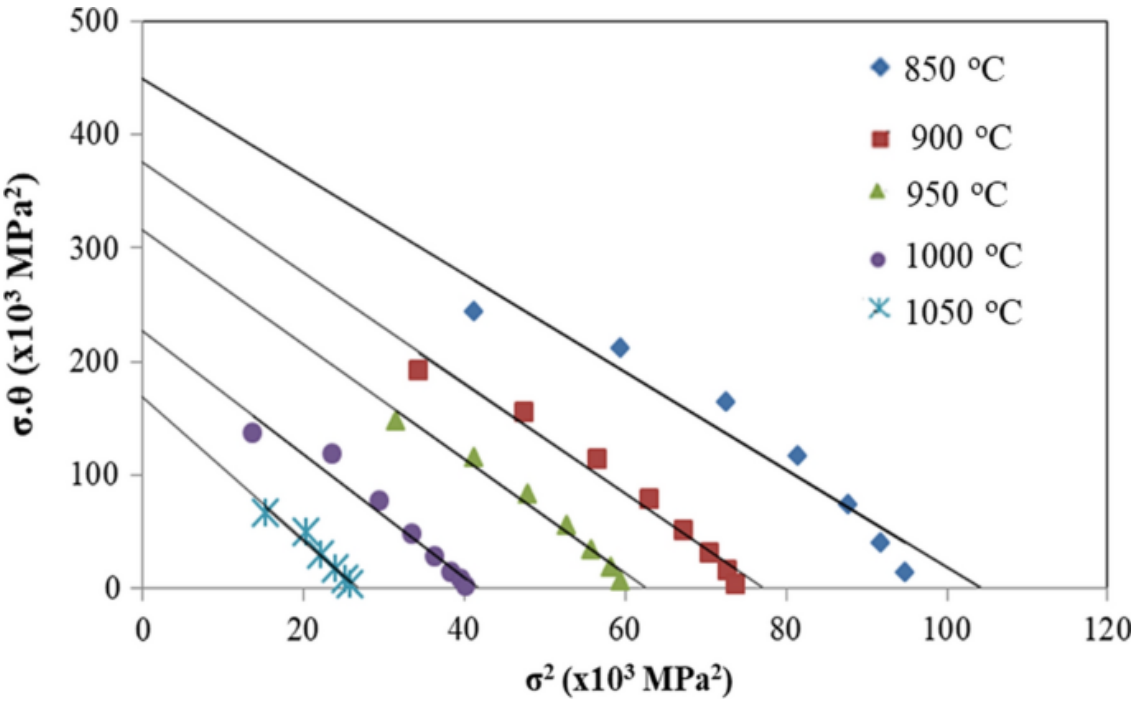

Fig. A1. Plot of $\sigma\theta$ against σ^2 to determine the values of A and B at a strain rate of 15 s^{-1}

Appendix 2: Derivation of the constants in the Avrami softening model

$$X = 1 - \exp\left[-r\left(\frac{\varepsilon}{\varepsilon_p}\right)^q\right] \tag{A4}$$

where the fractional softening

$$X_s = \left(\frac{\sigma_{sat} - \sigma}{\sigma_{sat} - \sigma_{ss}}\right) \tag{A5}$$

$$1 - X = \exp\left[-r\left(\frac{\varepsilon}{\varepsilon_p}\right)^q\right] \tag{A6}$$

$$\ln(1 - X) = -r\left(\frac{\varepsilon}{\varepsilon_p}\right)^q \tag{A7}$$

$$-\ln(1 - X) = r\left(\frac{\varepsilon}{\varepsilon_p}\right)^q \tag{A8}$$

$$\ln\left(-\ln(1 - X)\right) = \ln r + q\ln\left(\varepsilon - \varepsilon_p\right) \tag{A9}$$

Thus, the values of the constants r and q will be obtained from the plot of $\ln(-\ln(1-X))$ against $\ln(\varepsilon-\varepsilon_p)$ where $\ln r$ is the y-intercept and q the slope of the linear approximation of the corresponding plot. From the graph below $\ln r = 2.1875$ and hence $r = 8.9$ and $q = 1.7$ (Figure A2).

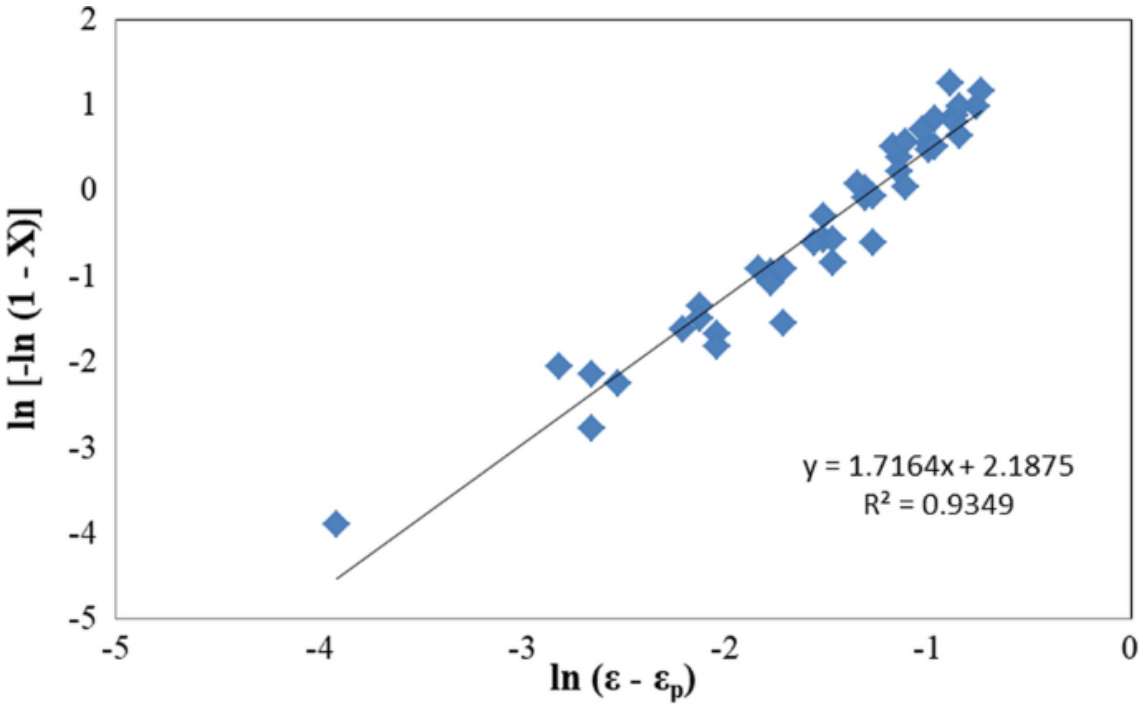

Fig. A2. Plot of $\ln(-\ln(1-X))$ against $\ln(\varepsilon-\varepsilon_p)$ to determine the values of r and q at a strain of 0.8, a strain rate of 15 s^{-1} and a temperature range of 850 °C to 1050 °C